

# Receiver Functions from Multiple-Taper Spectral Correlation Estimates

by Jeffrey Park and Vadim Levin

**Abstract** Teleseismic  $P$  waves are followed by a series of scattered waves, particularly  $P$ -to- $S$  converted phases, that form a coda. The sequence of scattered waves on the horizontal components can be represented by the receiver function (RF) for the station and may vary with the approach angle and azimuth of the incoming  $P$  wave. We have developed a frequency-domain RF inversion algorithm using multiple-taper correlation (MTC) estimates, instead of spectral division, using the pre-event noise spectrum for frequency-dependent damping. The multitaper spectrum estimates are leakage resistant, so low-amplitude portions of the  $P$ -wave spectrum can contribute usefully to the RF estimate. The coherence between vertical and horizontal components can be used to obtain a frequency-dependent uncertainty for the RF. We compare the MTC method with two popular methods for RF estimation, time-domain deconvolution (TDD), and spectral division (SPD), both with damping to avoid numerical instabilities. Deconvolution operators are often biased toward the frequencies where signal is strongest. Spectral-division schemes with constant water-level damping can suffer from the same problem in the presence of strong signal-generated noise. Estimates of uncertainty are scarce for TDD and SPD, which impedes developing a weighted average of RF estimates from multiple events. Multiple-taper correlation RFs are more resistant to signal-generated noise in test cases, though a “coherent” scattering effect, like a strong near-surface organ-pipe resonance in soft sediments, will overprint the  $P$ s conversions from deeper interfaces. The MTC RF analysis confirms the broad features of an earlier RF study for the Urals foredeep by Levin and Park (1997a) using station ARU of the Global Seismographic Network (GSN), but adds considerable detail, resolving  $P$ -to- $S$  converted energy up to  $f = 4.0$  Hz.

## Introduction

Receiver functions (RFs) are an important tool in the seismic investigation of the crust and upper mantle (Phinney, 1964; Burdick and Langston, 1977; Owens and Crosson, 1988). Receiver functions describe the tendency of an  $P$  wave, as it ascends toward a seismometer through the layers of the shallow Earth, to set off a chain of  $P$ -to- $S$  converted waves that accompany the reverberations of the main compressional wave. The oscillations within a receiver function are often taken to represent a succession of material interfaces beneath a given seismic station and have been used to study magma lenses within the crust (Sheetz and Schlue, 1992), the Moho (Sheehan *et al.*, 1995; Baker *et al.*, 1996; Sandvol *et al.*, 1998), the top of a subducting slab (Langston, 1981; Regnier, 1988; Eaton and Cassidy, 1996; Kosarev *et al.*, 1999), and other upper mantle elastic discontinuities (Kosarev *et al.*, 1984; Vinnik and Montagner, 1996; Dueker and Sheehan, 1997; Bostock, 1997; Gurrola and Minster, 1998). Numerical studies have suggested that complex  $P$  coda can be produced by reverberations with relatively simple crustal models with dipping interfaces or elastic aniso-

tropy (Cassidy, 1992; Levin and Park, 1997b; 1998; Savage, 1998). At frequencies of 1 Hz and above, however, there are serious concerns about the contamination of RF analysis by the scattered wave field (Abers, 1998), the portion of the  $P$ -wave coda that arises from multiple scattering and conversion in a strongly 3D crust.

Receiver functions are easy to define but difficult to compute in a reliable, robust manner. Favored methods to compute RFs use the record of vertical vibration on the seismogram, which contains mostly  $P$ -wave motion, to predict the records of radial- and transverse-horizontal seismic motion. The simplest way to accomplish this is by spectral division, a ratio of Fourier transforms for the different components:  $H_R(f) = Y_R(f)/Y_Z(f)$  and  $H_T(f) = Y_T(f)/Y_Z(f)$ . Here  $Y_Z(f)$ ,  $Y_R(f)$ , and  $Y_T(f)$  are the Fourier spectra of the vertical, radial, and transverse seismic components, respectively. The spectral-domain receiver functions  $H_R(f)$  and  $H_T(f)$  can be transformed into a prediction filter of  $P$ -to- $S$  scattered waves by performing the inverse Fourier transform on them.

Although simple to apply, raw spectral division is a bad

method. It is numerically unstable near the zeroes of  $Y_Z(f)$ . It also fails to account for seismic noise. To circumvent this, a modified spectral division is preferred, using a water level to avoid the zeroes of  $Y_Z(f)$  (Clayton and Wiggins, 1976; Ammon, 1991). Alternatively, one can deconvolve the horizontal seismic records from the vertical record in the time domain (Abers *et al.*, 1995; Gurrola and Minster, 1995) to compute the scattering prediction filter directly. Each of these techniques has shortcomings, as each tends to be band-limited in practice. A constant water level in spectral division obscures low-amplitude spectrum components. (Scaling the water level with the pre-event spectrum is a better strategy, but is not often applied.) Similarly, time-domain deconvolution tends to be dominated by the Fourier components with largest amplitude, in practice limiting many RF studies to use data low-passed at  $f \lesssim 0.5$  Hz. This has led to some spectacular images of upper-mantle discontinuities at 420- and 670-km depth (e.g., Dueker and Sheehan, 1997), but is problematic for probing fine-layered crustal structure.

How does one separate signal from signal-generated noise in RF analysis? The separation is not easy to achieve even in an abstract sense, because the signal in RF analysis is itself composed of scattered waves and often includes multiple reverberations. Popular options for enhancing signal in RF estimation involve the stacking, in various ways, of many seismograms from either different events at one station or from the same event recorded by a network or array of seismic stations (Gurrola *et al.*, 1995; Searcy *et al.*, 1996; Bostock and Sacchi, 1997; Dueker and Sheehan, 1997; Levin and Park, 1997a). Rather than rely only on stacking multiple records to suppress unwanted seismic energy, we develop in this paper an RF-computation algorithm that attempts to distinguish between “coherent” and “incoherent” scattering in 3-component records from single events. The method uses MTC (Kuo *et al.*, 1990; Vernon *et al.*, 1991) to estimate frequency-domain RFs in a manner that avoids the familiar numerical instabilities of spectral division (Ammon *et al.*, 1990). We develop an uncertainty estimate for the frequency-domain MTC RF. This allows the analyst to weigh RF estimates from different seismic events by their relative uncertainties, rather than resorting to an unweighted stack. The multiple-taper spectrum (MTS) estimators have optimal resistance to spectral leakage (Thomson, 1982; Park *et al.*, 1987). Therefore MTC RFs are resistant to the bias associated with the majority of incoming  $P$  waves that possess colored, not white, spectra.

MTC RF estimation does not address directly the interpretation of receiver functions in terms of Earth structure. The algorithm presented here represents only part of the geologic inference problem. We describe its technical details in the next section. The following section compares the MTC technique with published spectral-division and time-domain deconvolution RF estimators. A later section applies the MTC technique to estimate radial and transverse receiver functions for stations ARU and PET of the Global Seismo-

graphic Network (GSN). A final section summarizes our results.

### Multiple-Taper Receiver Functions

Assume we have three time series of vertical, radial, and transverse particle motion  $[u_R(n\tau), u_T(n\tau), u_Z(n\tau)] = \{u_n^R, u_n^T, u_n^Z\}_{n=0}^{N-1}$  with sampling interval  $\tau$  and duration  $T = N\tau$ . At each frequency,  $f$ , the  $K$  MTS estimates (Thomson, 1982; Lees and Park, 1995) are

$$Y_\gamma^{(k)}(f) = \sum_n u_n^\gamma w_n^{(k)} e^{i2\pi f n \tau}, \quad (1)$$

where  $\{w_n^{(k)}\}_{n=0}^{N-1}$  is the  $K$ th Slepian data taper for a user-chosen time-bandwidth product  $p$ . The parameter  $p$  scales the local average of spectral information about  $f$  (Park *et al.*, 1987; Vernon *et al.*, 1991), allowing at most  $K = 2p - 1$  statistically independent spectrum estimates (one per Slepian taper). In the multiple-taper approach, the choices of  $p$  and  $K$  quantify a trade-off between the resolution and variance of spectral estimates. For example, the  $Y_\gamma^{(k)}(f)$  can be combined to form coherence estimates  $C_R(f)$ ,  $C_T(f)$  between horizontal and vertical components:

$$C_R(f) = \frac{\sum_{k=0}^{K-1} (Y_Z^{(k)}(f) * Y_R^{(k)}(f))}{\left( \left( \sum_{k=0}^{K-1} (Y_R^{(k)}(f) * Y_R^{(k)}(f)) \right) \left( \sum_{k=0}^{K-1} (Y_Z^{(k)}(f) * Y_Z^{(k)}(f)) \right) \right)^{1/2}}$$

$$C_T(f) = \frac{\sum_{k=0}^{K-1} (Y_Z^{(k)}(f) * Y_T^{(k)}(f))}{\left( \left( \sum_{k=0}^{K-1} (Y_T^{(k)}(f) * Y_T^{(k)}(f)) \right) \left( \sum_{k=0}^{K-1} (Y_Z^{(k)}(f) * Y_Z^{(k)}(f)) \right) \right)^{1/2}}. \quad (2)$$

In the applications that follow, we fix time-bandwidth product  $p = 2.5$  and  $K = 3$ , so that the  $(C_R(f))^2$  and  $(C_T(f))^2$  can, for locally white spectral processes, be related to the  $F$  variance-ratio test with 2 and 4 degrees of freedom.

We identify the frequency-domain RFs  $H_R(f)$ ,  $H_T(f)$  with the damped spectral correlation estimators

$$H_R(f) = \frac{\sum_{k=0}^{K-1} (Y_Z^{(k)}(f) * Y_R^{(k)}(f))}{\left( \left( \sum_{k=0}^{K-1} (Y_Z^{(k)} * Y_Z^{(k)}) \right) + S_o(f) \right)}$$

$$H_T(f) = \frac{\sum_{k=0}^{K-1} (Y_Z^{(k)}(f) * Y_T^{(k)}(f))}{\left( \left( \sum_{k=0}^{K-1} (Y_Z^{(k)} * Y_Z^{(k)}) \right) + S_o(f) \right)} \quad (3)$$

The damping factor  $S_o(f)$  is a spectrum estimate of the pre-

event noise on the vertical component. The  $H_R(f)$ ,  $H_T(f)$  functions are analogous to the frequency response of a seismometer: complex-valued with (hopefully) a causal phase. Formal uncertainties on the frequency-domain RFs can be estimated under the assumption that the residual spectral variance on the horizontal components (i.e., the part uncorrelated with the vertical component) can be used to estimate the overall noise level. The variance of the RF scales with its squared amplitude:

$$\begin{aligned}\text{var}(H_R(f)) &= \left( \frac{1 - (C_R(f))^2}{(K - 1)(C_R(f))^2} \right) |H_R(f)|^2 \\ \text{var}(H_T(f)) &= \left( \frac{1 - (C_T(f))^2}{(K - 1)(C_T(f))^2} \right) |H_T(f)|^2.\end{aligned}\quad (4)$$

The formal uncertainty is small when coherence is near unity and large for smaller coherences. For  $(C_\gamma(f))^2 = 1/K$ , the expectation for random noise,  $\text{var}(H_\gamma(f)) = |H_\gamma(f)|^2$ .

The formal uncertainty estimate offers a way to form composite RFs in the frequency domain from different seismic records in a weighted linear combination. We use the inverse variances of the individual RFs as weights so that poorly constrained  $H_\gamma(f)$  influence the weighted sum less than do RFs with smaller uncertainty. At frequencies where the coherence between vertical and horizontal seismic components is low, one can presume that noise has obscured their relationship. In our experience with the MTC RF-estimation technique, the vertical-radial-transverse coherences vary strongly with frequency, in a manner largely unpredictable from either the signal-to-noise ratio or a visual perusal of the data. Because the incoherent portion of the horizontal components is typically too large to be attributed to the pre-event background noise level, we attribute the coherence variations to signal-generated noise, that is, scattered waveforms that correlate poorly, in a statistical sense, with the incoming  $P$  wave. Simple side-scattered  $Pp$  and  $Ps$  body waves could, in principle, retain coherence with the incoming  $P$  wave, so the incoherent signal is most likely a combination of multiply scattered body waves and body-to-surface wave conversions.

We compute time-domain MTC receiver functions  $H_R(t)$  and  $H_T(t)$  via an inverse Fourier transform of  $H_R(f)$  and  $H_T(f)$ . The time-domain RFs represent so-called prediction filters of horizontal motion, as generated by impulsive vertical-component motion. In the time domain there are no formal uncertainties on the RFs, but fluctuations in the RF at negative times offer a visual assessment of uncertainty in the wiggles that follow. When frequency-domain RFs from multiple data records are combined in a weighted average, any spurious precursory portion of the prediction filter tends to decrease in the composite time-domain RF. In principle, formal time-domain RF uncertainties can be estimated with bootstrap-resampling of the available seismic records. In this article we illustrate the RF uncertainties informally by com-

paring the consistency of bin-averaged RFs over both epicentral distance and backazimuth.

To avoid Gibbs-effect ringing in the RF, we low-pass the spectrum up to a user-specified cutoff frequency,  $f_c$ , with a cosine-squared function, analogous to the Hanning taper in time series analysis (Park *et al.*, 1987). Other functional choices can be made, but both  $\cos^2\left(\frac{\pi f}{2f_c}\right)$  and its first derivative vanish at  $f_c$ , which is sufficiently bodacious for our applications. With this filter, RFs with  $f_c = 2$  Hz include significant information only up to  $\sim 1.3$  Hz, with half-amplitude at 1 Hz. We normalize  $H_R(t)$  and  $H_T(t)$  with the factor  $2f_N/f_c$ , where  $f_N = 1/(2\tau)$  is the Nyquist frequency, in order to preserve the amplitude of converted phases.

In the context of receiver functions, the time-bandwidth product,  $p$ , trades off with the frequency resolution of  $H_R(f)$  and  $H_T(f)$ . Roughly speaking, spectral variation over small intervals in the frequency-domain corresponds with widely spaced features in the time domain. Therefore, the resolution of  $H_R(f)$ ,  $H_T(f)$  influences the length of the prediction filters  $H_R(t)$ ,  $H_T(t)$  that can be retrieved faithfully. In test analyses we have found that  $Ps$  converted-wave pulses in seismic data are difficult to retrieve with the MTC algorithm if their delay times,  $t$ , greatly exceed  $T/2p$ , where  $T$  is the duration of the seismogram analyzed. For instance, with  $p = 2.5$  and  $T = 50$  sec, the time-domain RF tends to low amplitude for delay times,  $t$ , much greater than 10 sec. Analysis of longer data records can extend the useful length of the RF. Reducing the time-bandwidth product,  $p$ , would also extend the RF, at the cost of increased spectral leakage in the spectrum estimates  $Y_Z^{(k)}(f)$ ,  $Y_R^{(k)}(f)$ , and so on, making necessary adaptive weighting in the multiple-taper estimates (Thomson, 1982; Park *et al.*, 1987). Optimal choices of  $p$ ,  $K$ , and  $T$  will surely vary with epicentral distance, the seismic observatory, and the time delay of the targeted  $Ps$  conversion. We have found  $p = 2.5$  and  $K = 3$  adequate for  $Ps$  conversions in the upper 100 km of the crust and mantle (e.g., Levin and Park, 2000). Different parameter choices, for example, smaller  $p$ , may optimize retrieval of late-arriving  $Ps$  conversions from the 420- and 670-km discontinuities.

Figures 1 and 2 demonstrate the MTC algorithm with a synthetic test, contrived from  $P$ -wave data recorded at GSN station PET (Petropavlovsk-Kamchatsky, Russia) with sample time  $\tau = 0.05$  sec, from the 6 September 1993 earthquake near New Ireland ( $m_b = 6.2$ ). We generated artificial horizontal-component seismic records via spike-convolution, that is, by summing time-shifted copies of the vertical component seismic record (Fig. 1). The spike functions for the radial and transverse traces are

$$\begin{aligned}S_R(t) &= 0.3\delta(t) + 0.1\delta(t - 4) - 0.1\delta(t - 5) \\ S_T(t) &= -0.1\delta(t) + 0.1\delta(t - 1) + 0.1\delta(t - 5),\end{aligned}\quad (5)$$

corresponding to  $Ps$  converted phases at  $t = 1, 4$ , and 5 sec.

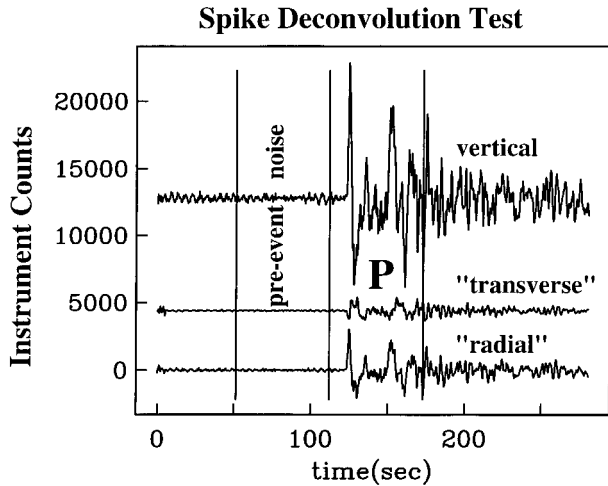


Figure 1. Test case to demonstrate MTC RF estimation, contrived from a  $P$  wave recorded at GSN station PET (Petropavlovsk-Kamchatsky, Russia), sampled at  $\tau = 0.5$  sec. The horizontal traces are explicit convolutions of the vertical data trace with a spike series at a handful of time lags; see equation (5).

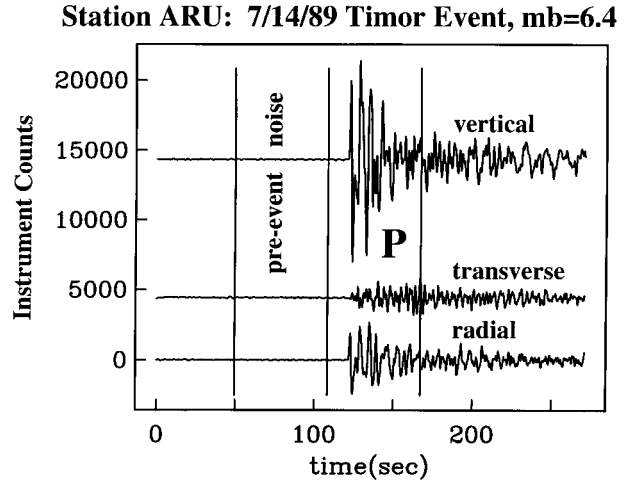


Figure 3.  $P$  wave from the Bastille Day (14 July), 1989 event ( $m_b = 6.4$ ) near Timor, Indonesia, as recorded at GSN station ARU (Arti Settlement, Russia). The 57-sec time window for RF analysis is marked by vertical lines. The spectra of an equal-length time window of pre-event noise, also marked, is estimated to determine damping parameters for the MTC regression.

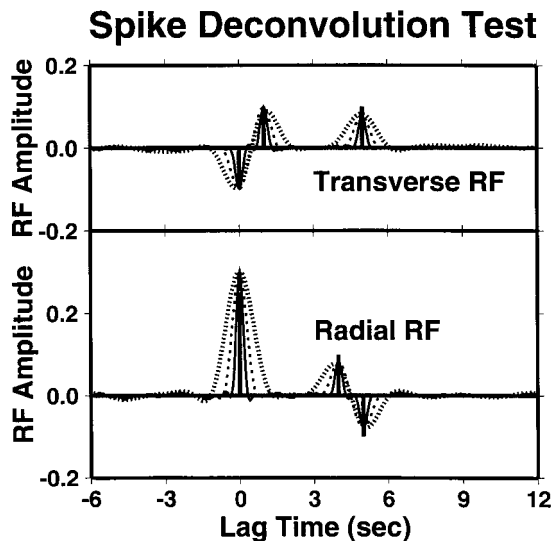


Figure 2. MTC RF estimates for the data series shown in Figure 1. The thick line graphs the true spike convolution function. The solid line graphs the RFs with frequency cutoff  $f_c = 3.0$  Hz. The coarsely dashed line graphs the RFs with frequency cutoff  $f_c = 1.5$  Hz. The finely dashed line graphs the RFs with frequency cutoff  $f_c = 0.8$  Hz.

Figure 2 shows the MTC RFs for frequency cutoffs  $f_c = 0.8, 1.5, \text{ and } 3.0$  Hz.

Figures 3, 4, and 5 illustrate the computation of the MTC RF for a  $P$  wave from a shallow earthquake in Timor ( $m_b = 6.4, h = 10$  km) on Bastille Day 1989 (14 July), recorded

at GSN station ARU (Arti Settlement, Russia). Although signal-to-noise is high, the  $P$  wave train is not an ideal candidate for RF estimation because it is extended in time rather than impulsive (Fig. 3). We analyse a 57-sec record at 20 samples/sec, padding the 1140 data points with zeroes to apply a 2048-point fast Fourier transform. The signal and pre-event spectra are compared in Figure 4 and show that the signal-to-noise ratio is high at frequencies  $f > 1$  Hz, even though the  $P$  wave is dominated by frequencies  $f < 0.7$  Hz. The coherences are variable but often near unity even where the spectrum has low amplitude. Note, however, that coherence between horizontal and vertical components can be low in bandpasses where the nominal signal-to-noise ratio is high. We interpret this paradox as the effect of signal-generated noise, for example, incoherent multiply scattered energy. The error bars on  $H_R(f)$  and  $H_T(f)$  in Figure 5 demonstrate that the radial RF is better constrained than the transverse RF, reflecting the higher average coherence between radial and vertical motion. Nevertheless, a sequence of pulses in the first 6 sec of the transverse RF  $H_T(t)$  can be reconstructed from spectral ratios at  $f > 0.5$  Hz. These pulses are constructed from spectral information at frequencies roughly twice those that dominate the incoming  $P$  wave. Although there is no formal uncertainty estimate for the time-domain RF, the amplitude of  $H_R(t), H_T(t)$  for  $t < 0$ , that is, the noncausal part of the prediction filter, gives a qualitative feel for the uncertainty. In this example,  $H_R(t), H_T(t)$  have largest amplitude for lags  $t \leq 6$  sec, suggesting that forward scattering from the Moho and crustal interfaces dominates the  $P$  coda. Both the negative excursion at  $t \sim 2$  sec in  $H_R(t)$  and the negative-positive derivative pulse in

## Station ARU: 7/14/89 Timor Event, mb=6.4

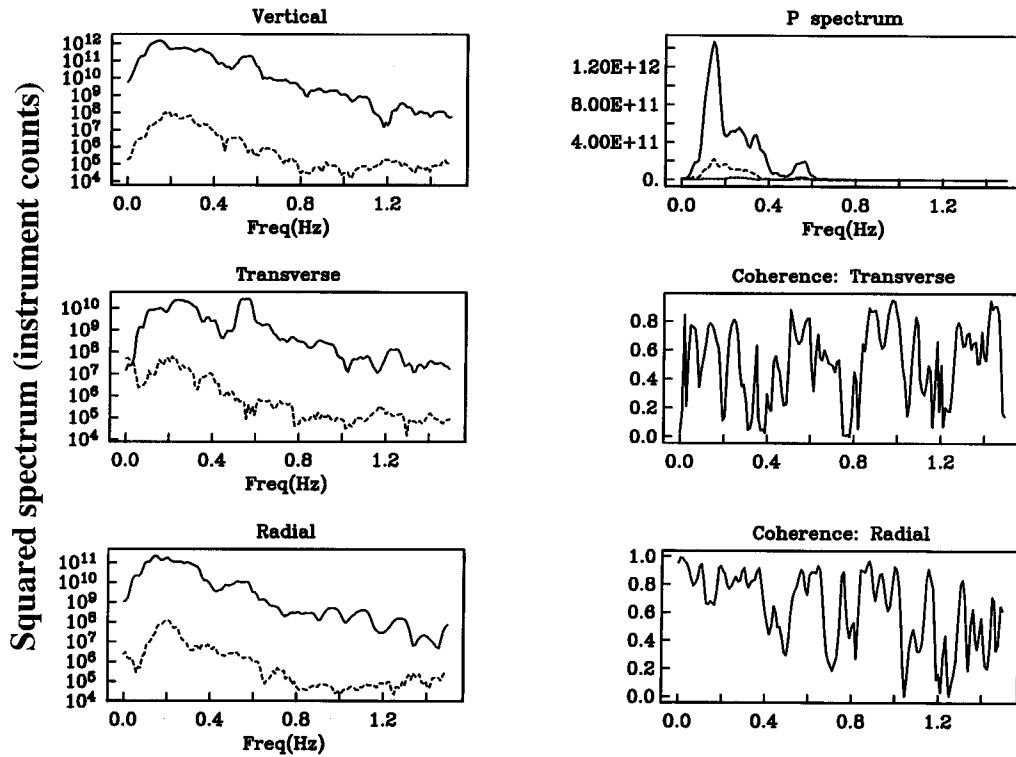


Figure 4. First step in MTC RF estimation, applied to the  $P$  wave shown in Figure 3. Log-linear plots in the left column plot the  $P$ -coda spectra (solid) versus pre-event noise spectra (dashed) for the three particle-motion components. In the top-right panel, the  $P$ -coda spectrum estimates of the vertical (solid), radial (coarse dash), and transverse (fine dash) components are superimposed. Also in the right column are plotted the squared coherence  $C^2(f)$  of the transverse and radial components, respectively, with the vertical component.

$H_T(t)$  at 4- to 5-sec delay were noted by Levin and Park (1997a) in RFs for ARU, computed using simultaneous inversion of multiple events with time-domain deconvolution (not with the MTC algorithm).

### Comparison with Popular Receiver Function Estimators

We compare the MTC RF estimator with two popular techniques: (1) spectral division with water-level damping (Ammon, 1990) and (2) time-domain deconvolution (e.g., Abers *et al.*, 1995). Spectral division estimates a frequency-domain RF that can be lowpassed and normalized for easy comparison with the MTC technique. The bandpass and normalization of the time-domain-deconvolution RF is more difficult to manipulate, so amplitude comparisons can be misleading. However, the contrasts between techniques are more substantive than normalization comparisons.

For the spectral-division (SPD) RF estimator, we apply the formula

$$H_\gamma(f) = Y_\gamma(f)(Y_Z(f))^*/\max(|Y_Z(f)|^2, W), \quad (6)$$

where the water-level damping  $W = \lambda \sum_{n=0}^{N-1} (u_n^Z)^2$  scales with the root mean square (rms) amplitude of the vertical particle motion. Experience shows that the primary source of distortion in the RF arises from signal-generated noise, so we scale the damping by the event amplitude, not the pre-event amplitude. The SPD RF can be expressed in the time domain via an inverse Fourier transform. Similar to the MTC RF estimator, we apply a cosine-squared taper in the frequency domain up to a cutoff frequency  $f_c$ .

For time-domain deconvolution (TDD), we solve a least-squares problem for a causal  $M$ -point prediction filter  $\mathbf{s} = \{s_m\}_{m=0}^{M-1}$  using an  $N \times M$  kernel matrix  $\mathbf{G}$ . The  $M$  columns of  $\mathbf{G}$  are time shifted copies of the  $N$ -point vertical component record  $\{u_n^Z\}_{n=0}^{N-1}$ , preceded by zeroes to enforce causality. The mathematical problem can be expressed

$$\mathbf{G} \cdot \mathbf{s} = \mathbf{d} \quad (7)$$

with either the radial or transverse particle-motion record in

## Station ARU: 7/14/89 Timor Event, mb=6.4

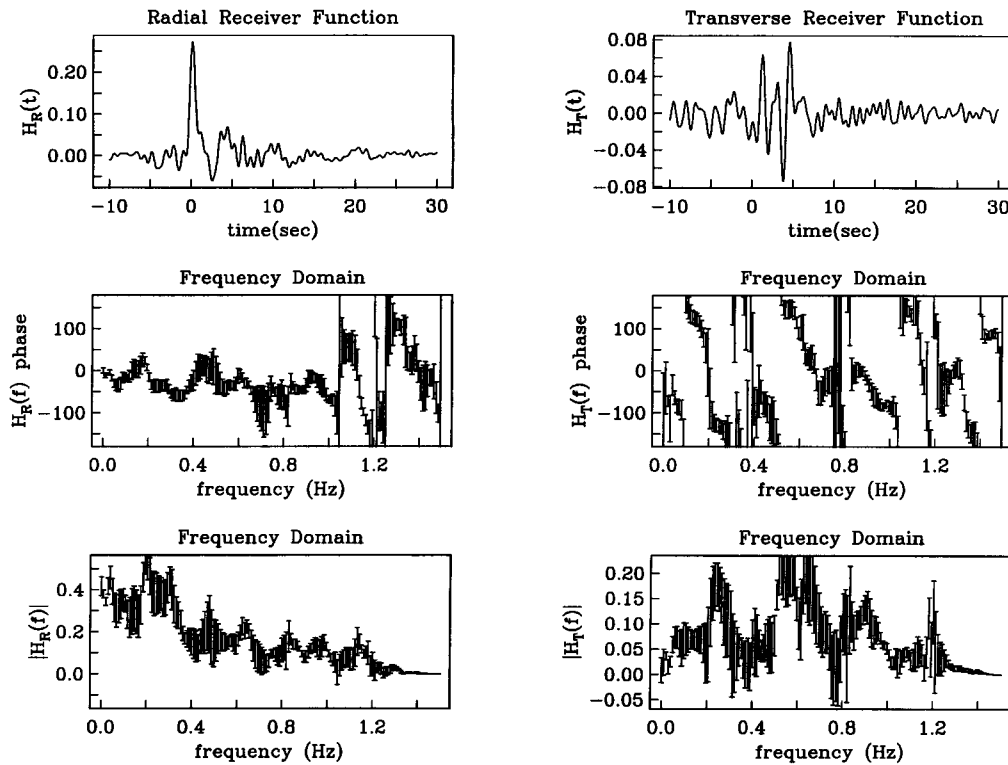


Figure 5. Second step in MTC RF estimation, applied to the  $P$  wave shown in Figure 3. The left column graphs the radial RF. The right column graphs the transverse RF. The top row graphs the RFs in the time domain. The center and bottom rows graph the phase and amplitude, respectively, of the complex-valued RF in the frequency domain, with error bars.

the data vector  $\mathbf{d}$ . The solution vector  $\mathbf{s}$ , which estimates a time-domain RF, is computed using a damped generalized inverse

$$\mathbf{s} = (\mathbf{G}^T \cdot \mathbf{G} + W\mathbf{I})^{-1} \cdot \mathbf{G}^T \cdot \mathbf{d} \quad (8)$$

where damping scalar  $W = \lambda \sum_{n=0}^{N-1} (u_n^Z)^2$  sums the vertical-component motion to scale the  $M \times M$  identity matrix  $\mathbf{I}$ . We solved for a 32-sec prediction filter to mimic the filter length afforded by the other methods. We also Fourier-transformed the time-domain RF to compare methods in the frequency domain.

Figure 6 shows that both comparison techniques are able to retrieve the artificial spike-convolution test case shown in Figure 1. Only results for the radial component are shown. The choice of the scale factor  $\lambda$  for damping in both SPD and TDD techniques is typically governed by subjective assessments of numerical stability, so we tested different values. The SPD RFs are computed for  $\lambda = 0.1$ , with frequency cutoffs  $f_c = 0.8, 1.5,$  and  $3.0$  Hz. The three TDD RFs are computed for  $\lambda = 0.01, 0.1,$  and  $1.0$ . Time-domain deconvolution is strictly causal, set to vanish at times  $t < 0$ . This restriction seems to force an amplitude mismatch between

the zero-lag peak and the peaks that follow. For modest damping, the TDD RF adequately retrieves the major features of the spike-convolution. A spurious downswing is introduced with the heaviest damping ( $\lambda = 1.0$ ).

For real data, the results of popular RF-estimation methods diverge from those of the MTC RF estimator. To reduce bias from signal-generated noise, both SPD and TDD techniques required larger damping ( $\lambda = 0.3$  and  $5$ , respectively) than required for the contrived spike-convolution example. Figures 7 and 8 show computed RFs for the Bastille Day 1989 event near Timor in both the time and frequency domain. No error bars are available in the frequency domain for the SPD and TDD methods. However, the scatter in the amplitude and phase of  $H_R(f)$  and  $H_T(f)$  suggests significant levels of uncertainty. Time-domain RFs from all methods share some qualitative features in the first  $\sim 5$  sec. All share a downswing on the radial RF at  $t = 2.5$  sec, suggesting  $P$ -to- $S$  conversion at the top of a midcrustal low-velocity layer. All share an oscillation on the transverse RF at  $t \sim 4$ – $5$  sec, interpreted by Levin and Park (1997a) as conversions at the top and bottom of a basal crustal layer. However, here the similarities end. Both SPD and TDD algorithms lead to prediction filters  $H_R(t)$  and  $H_T(t)$  with longer durations at sig-

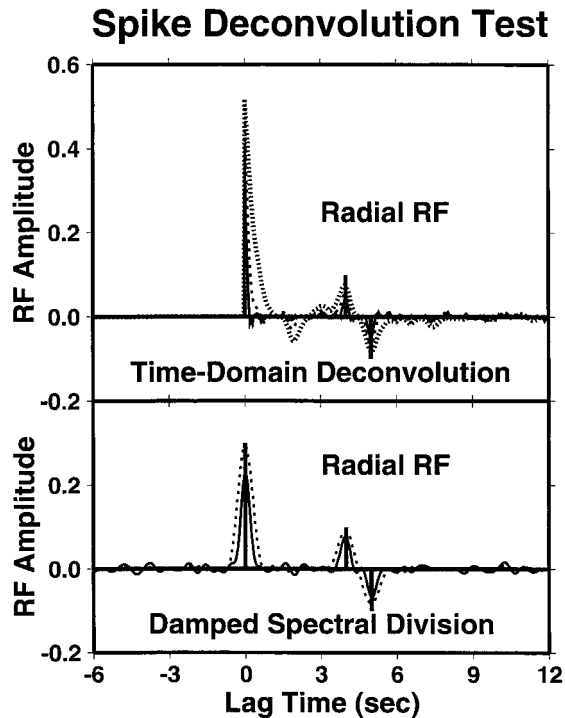


Figure 6. RF estimates for the data series shown in Figure 1, using time-domain deconvolution (TDD) and spectral division with water-level damping (SPD). The thick line graphs the true spike convolution function. The SPD RFs are plotted with frequency cutoffs  $f_c = 3.0$  Hz (solid), 1.5 Hz (coarse dash), and 0.8 Hz (fine dash), and damping scale factor  $\lambda = 0.1$ . The TDD RFs are plotted for three different values of the damping scale factor  $\lambda = 0.01$  (solid), 0.1 (coarse dash), and 1.0 (fine dash).

nificant amplitude, compared to the MTC RF. The transverse RFs are highly oscillatory, with significant amplitude at  $t < 0$ , suggesting that they are not robust.

The MTC RF estimate involves only two free parameters, the time-bandwidth product,  $p$ , and a frequency cutoff. In spectral division RF estimation, a user-chosen damping parameter,  $\lambda$ , takes the place of  $p$ , but  $\lambda$  does a poorer job of reducing the influence of zero-crossings in the seismic spectra. Figure 7 suggests that  $H_R(f)$  and, especially,  $H_T(f)$  in the SPD method can be distorted by a handful of spurious spectral ratios at isolated frequencies. Water-level damping can ameliorate the effects of these bad points, but at the cost of overdamping the RF at other frequencies. Using spectral correlation and coherence estimates to estimate  $H_V(f)$  as an alternative to spectral ratios broadens the frequency bandwidth over which spectral information is gleaned and greatly reduces the bias introduced by any one point in the Fourier spectrum.

Our comparison is somewhat unfair to the time-domain deconvolution method, which has been applied with some success by many researchers, including the present authors. Low-passed TDD RFs using multiple events and sources can

be migrated and stacked to image upper mantle conversions, for example, as done by Dueker and Sheehan (1997). Alternatively, TDD can be restricted to earthquakes with short time durations, and prediction filters  $H_R(t)$ ,  $H_T(t)$  no longer than 5–10 seconds solved for (e.g., Levin and Park, 1997a). One also must choose the damping parameter  $\lambda$  for the matrix inversion ([equation 8]) so that there are several potential sources of subjectivity in the algorithm. The frequency-dependent RF amplitude in Figure 8 indicates that the damping needed to overcome signal-generated noise can lead to a highly low-passed RF.

The comparisons in this section favor the MTC RF estimator as a tool to investigate shallow Earth structure, especially crustal structure. Such a conclusion can be rationalized with both technical arguments about numerical stability and the more general assertion that a spectral coherence estimator is more likely to reject the portion of a seismic data series that arises from “incoherent” scattering. This is not, however, a rigorous, incontrovertible line of reasoning. As with most methods of inference in complex geologic systems, the best argument for a method’s utility is its ability to obtain consistent, interpretable results in test cases. We explore these in the next section.

## Data Examples

We have estimated distance- and backazimuth-dependent receiver functions for the broadband stations ARU (Arti Settlement, Russia) and PET (Petropavlovsk-Kamchatsky, Russia) of the Global Seismographic Network (GSN). ARU lies above the foredeep of an ancient (Paleozoic) continental suture zone, marked by the north–south trending Ural Mountains. PET lies in the shadow of arc volcanoes above the active Kamchatka subduction zone in the northwest Pacific (Gorbatov *et al.*, 1997). PET is sited within a granitic outcrop surrounded by a thick sequence of accretionary-wedge facies, possibly mixed with tephra layers.

Levin and Park (1997a) identified a strongly anisotropic lower-crustal layer beneath station ARU, using time-domain deconvolution on 166 selected seismic records from 1990 to 1996. For reference, the model derived in that study is listed in Table 1. Using the new RF-estimation technique, we were able to utilize data from 442 seismic events with  $M = 6.3$  or greater during 1989–98, including 112 core-refracted high-frequency *PKP* and *PKiKP* phases from events more distant than  $\Delta = 95^\circ$ . Because the horizontal components at ARU suffer slow drift over time, we high-passed the records at  $f = 0.01$  Hz before MTC RF analysis. The duration of *P*-coda analyzed varies from 50 to 100 sec, depending on the apparent source-pulse duration and the separation of interfering body waves with phase velocities that differ greatly, for example, *PKP* and *PP*. Some events have significant ratios of signal to pre-event noise over only a portion of the frequency band of interest (0–6 Hz). A larger potential problem is the marginal coherence between horizontal and vertical components, due to signal-generated noise, on many

## Station ARU: 7/14/89 Timor Event, mb=6.4

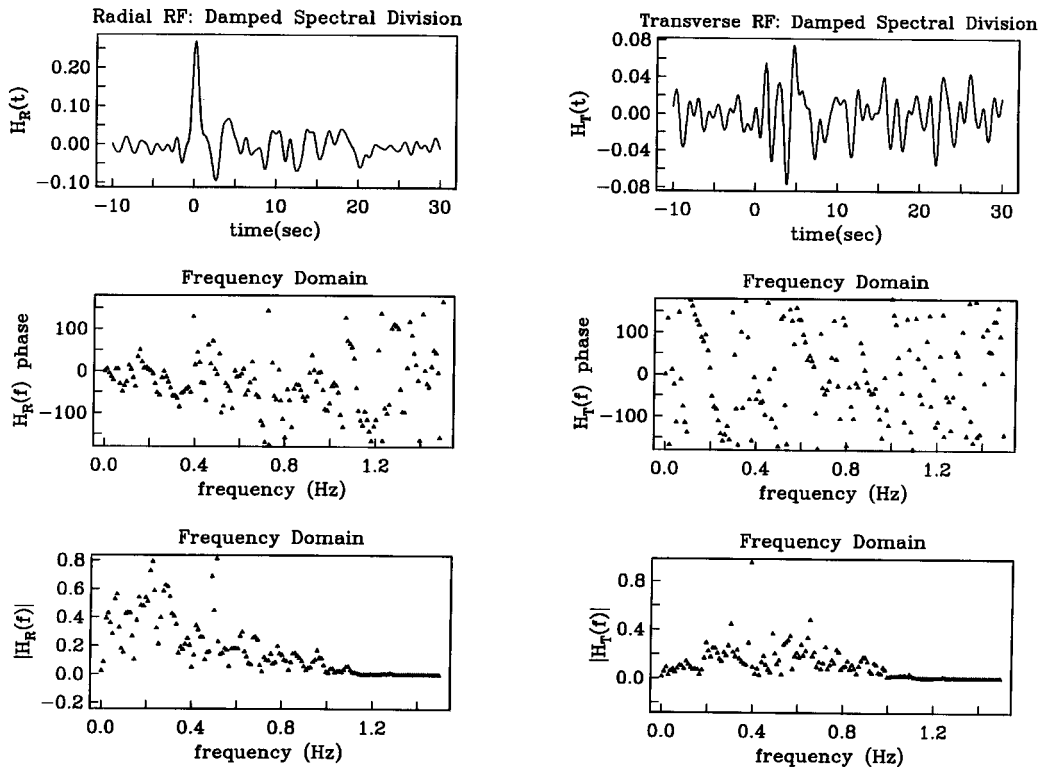


Figure 7. Damped spectral division RF estimates for the Bastille Day, 1989,  $P$  wave shown in Figure 3. The left column graphs the radial RF. The right column graphs the transverse RF. The top row graphs the RFs in the time-domain. The center and bottom rows graph the phase and amplitude, respectively, of the complex-valued RF in the frequency domain. The RFs are computed for frequency cutoff  $f_c = 1.5$  Hz and damping parameter  $\lambda = 0.3$ .

records (Fig. 9). At  $f > 1$  Hz, the average of squared coherence over 442 records ( $C^2(f) \sim 0.40$ – $0.45$ ) is not much larger than expected for random white noise time series ( $C^2(f) = 1/3$ ). Even for  $f < 1$  Hz, the averaged  $C_T^2(f)$  exceeds 0.5 at only a handful of frequencies. At face value this consigns more than half the transverse-component data variance to signal-generated noise. On the other hand, an average  $C^2(f) = 0.4$  over 442 records is highly significant (99.9999% confidence for nonrandomness in a white-noise context), so in principle there is useful signal over the entire frequency range 0–6 Hz.

We bin-averaged frequency-domain RFs from individual records in overlapping  $10^\circ$  intervals of either epicentral distance,  $\Delta$ , or backazimuth,  $\psi$ . The bins are spaced at  $5^\circ$  intervals. The bin-averaging scheme allows the RFs for a particular event to influence composite RFs in two adjoining bins. The transverse RF changes polarity with backazimuth,  $\psi$ , so to examine the moveout of the RFs with epicentral distance, we summed only events in the backazimuth range  $50$ – $150^\circ$ . (This includes the western Pacific subduction zones.) When the composite RFs for ARU are plotted against epicentral distance  $\Delta$  (Fig. 10), the moveout of the  $P$ -to- $S$

converted wave at the Moho ( $\sim 4$ - to  $5$ -sec time delay) is mildly evident for  $\Delta < 60^\circ$ . The  $P_s$  delay is greater for closer events, because the  $P$ -wave incidence angle is more shallow and the converted wave must travel a longer path from the base of the crust to the seismometer. Note that the RFs obtained from mantle  $P$  waves at shallow incidence ( $\Delta < 30^\circ$ ) appear consistent with those computed for more steeply incident  $P$  waves. A weaker converted phase appears at 9–10 sec delay and is more visible on the transverse RF sweep. This phase shares the  $\Delta$ -moveout of the Moho-converted phase. A crustal multiple would have moveout in the opposite sense (Bostock, 1997). This  $P_s$ -converted energy may arise from a mantle interface related to the multilayered anisotropic mantle model derived by Levin *et al.* (1999) to explain shear-wave splitting at ARU, but the poor depth resolution of splitting data would make direct comparison difficult. At  $t = 0$ , there is a distance-dependent amplitude modulation of the radial RF  $H_R(t)$ . The largest  $H_R(0)$  is found for closer events, in which the incoming  $P$  wave has shallow incidence and a substantial radial projection. The minimum radial RF amplitude occurs at epicentral distances beyond  $100^\circ$ , where  $PKP$  waves are steeply incident.

## Station ARU: 7/14/89 Timor Event, mb=6.4

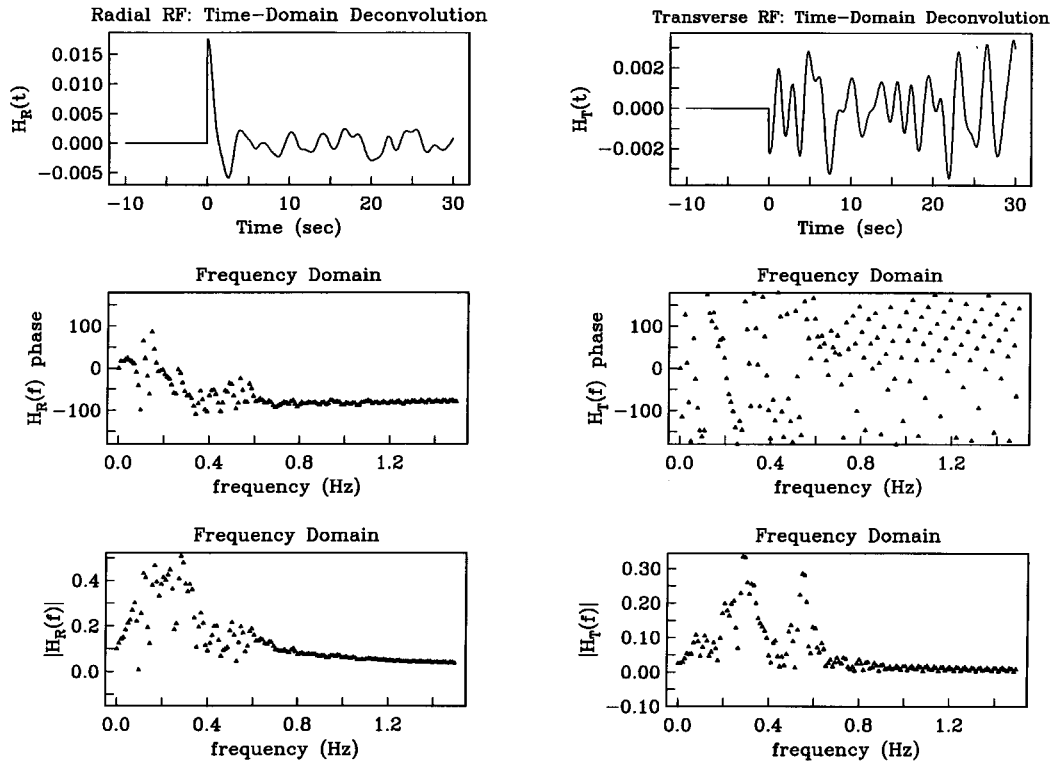


Figure 8. Time-domain deconvolution RF estimates for the Bastille Day, 1989,  $P$  wave shown in Figure 3. The left column graphs the radial RF. The right column graphs the transverse RF. The top row graphs the RFs in the time domain. The center and bottom rows graph the phase and amplitude, respectively, of the complex-valued RF in the frequency domain. The RFs are computed for damping parameter  $\lambda = 5$ . Smaller  $\lambda$  lead to large spurious oscillations in the RF for  $t > 10$  sec.

Table 1

Anisotropic Crust Consistent with Receiver Functions at ARU (Levin and Park, 1997a)

depth km	$V_p$ km/s	$V_s$ km/s	B %	E %	$\theta^\circ$	$\phi^\circ$	$\rho$ g/cm <sup>3</sup>
1	5.00	2.95	-15	0	45	345	2.1
20	6.40	3.70	0	0	-	-	2.3
23	5.8	3.30	0	0	-	-	2.3
33	6.60	3.80	0	0	-	-	2.6
40	7.60	4.40	-15	-15	65	230	3.0
$\infty$	8.00	4.6	0	0	-	-	3.3

Depth indicates the bottom of each layer. The parameters B and E scale peak-to-peak variations of  $V_p$  and  $V_s$ , respectively, each with  $\cos 2\psi$  dependence (Park, 1996). Angles  $\theta$  (tilt from vertical) and  $\phi$  (strike CW from N) define the symmetry axes.

The backazimuth sections for radial and transverse composite RFs (Fig. 11) confirm the anisotropic model of Levin and Park (1997a) for the crust beneath this station. A strong negative pulse on the radial RF at 2.5-sec delay indicates a midcrustal seismic low-velocity zone of some kind. There is also a strong derivative-pulse on the transverse RF that suffers amplitude polarity reversals with backazimuth,  $\psi$ , at

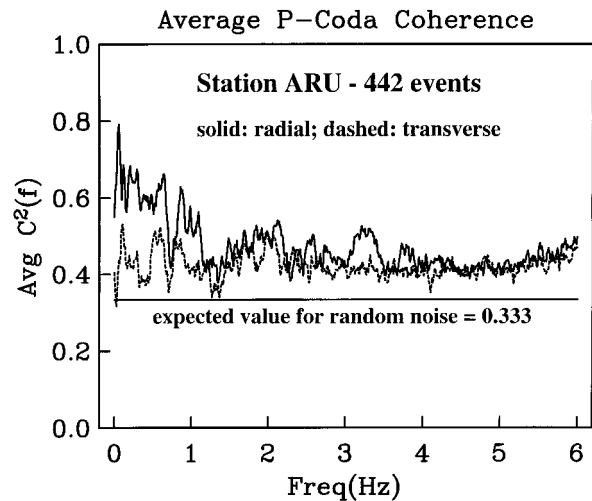


Figure 9. Average squared coherence  $C^2(f)$  at GSN station ARU for teleseismic  $P$ -coda from 442 seismic events with magnitude  $M \geq 6.3$ , between the vertical and radial (solid line) and transverse (dashed line) horizontal components of seismic motion.

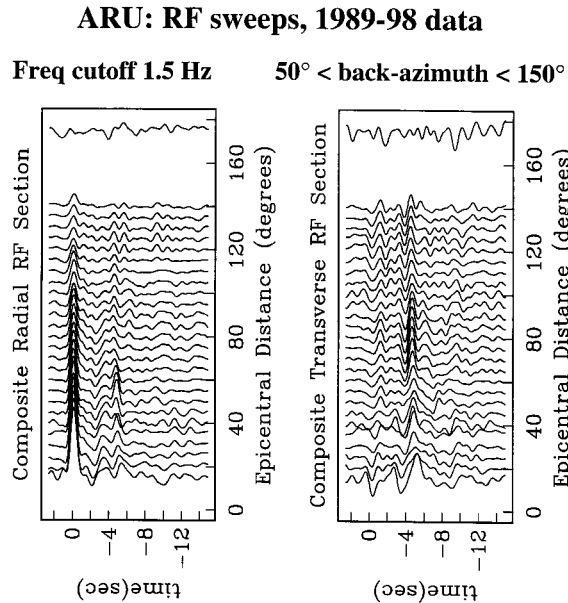


Figure 10. Composite RFs at ARU for frequency cutoff  $f_c = 1.5$  Hz, plotted against epicentral distance  $\Delta$ . Only events in the backazimuth range  $50\text{--}150^\circ$  contribute to the composite RFs. The composite RFs are computed from a weighted sum of single-event MTC RFs for events in a bin width  $\delta\Delta = 10^\circ$ . The composite RFs are computed with a spacing in  $\Delta$  of  $5^\circ$ , so data from each seismic event influences two adjacent bin averages.

roughly  $50^\circ$  and  $230^\circ$ . Levin and Park (1997a) modeled this behavior with two interfering  $P_s$  converted phases from the boundaries of a strongly anisotropic lower crustal layer with seismic velocity consistent with a steeply tilted fine-layered mixture of crustal metapelites and mantle peridotites. On the radial RF sweep, these two  $P_s$  phases interfere constructively, leading to a double-bump whose relative amplitudes vary somewhat with backazimuth,  $\psi$ . The Moho  $P_s$  phase in the radial RF sweep has peak amplitude near  $\psi = 50^\circ$ . This amplitude modulation is consistent with  $P_s$  conversion at an interface where one or both sides are anisotropic. Although several large Moho-converted  $P_s$  amplitudes are also observed near  $\psi = 230^\circ$ , the plot in Figure 11 is less coherent. In these backazimuth bins, earthquakes are distributed unevenly with epicentral distance, some bins dominated by nearby events, others by events more distant. The mix of epicentral distances in the data set shifts the RF peaks in delay time, particularly the Moho  $P_s$  conversion.

Overall, the RF sweeps computed with MTC appear more densely sampled and less cluttered than the TDD composite RFs presented by Levin and Park (1997a), more than one would expect from simply enlarging the data set. The greyscale plots in Figure 12 focus on short delay times in the RFs and suggest that the MTC RF estimate can be extended to higher frequency. With  $f_c = 6.0$  Hz, the RFs incorporate spectral information nearly up to the antialias filter

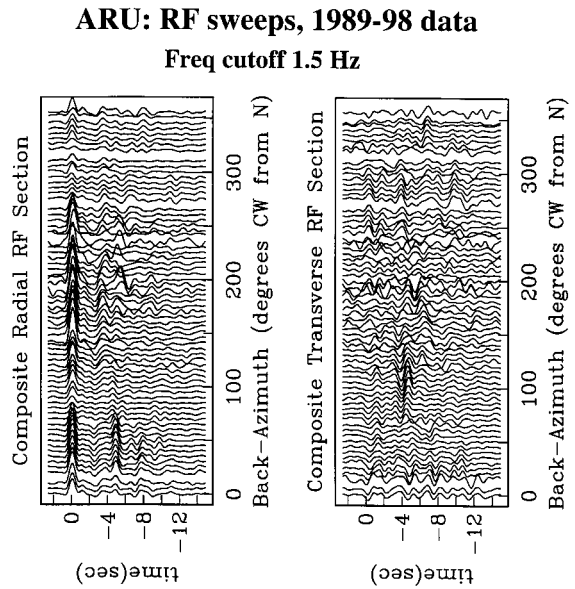


Figure 11. Composite RFs at ARU for frequency cutoff  $f_c = 1.5$  Hz, plotted against backazimuth,  $\psi$ . The composite RFs are computed from a weighted sum of single-event MTC RFs for events in a bin width  $\delta\psi = 10^\circ$ . The composite RFs are computed with a spacing in  $\psi$  of  $5^\circ$ , so data from each seismic event influences two adjacent bin averages. A handful of underpopulated bin averages were contaminated by long-period drift of the ARU horizontal components, and were excised from the graph. This figure can be compared with Figure 2 of Levin and Park (1997a) to assess the added resolution of the MTC RF estimator.

of the 20 samples/sec broadband data stream. The radial and transverse RF sweeps over epicentral distance reveal many sharp arrivals that appear as vertical streaks in the greyscale plots: dark for positive polarity, light for negative polarity. A full interpretation of the high-frequency RFs at ARU is beyond the scope of this article, but several features are worth noting. The Moho  $P_s$  conversion appears as a sharp pulse, suggesting a thin crust-mantle transition. In addition, the positive-polarity Moho  $P_s$  conversion at  $t = 5$  sec has a small downswing that follows it on the radial RF for  $\Delta > 60^\circ$ , suggesting complexity in the interface. The top of the basal crustal layer, placed at 33-km depth by Levin and Park (1997a), appears less sharp than the Moho. The low-frequency so-called interface may be a more gradational geologic structure. The transverse RF appears to lose its robustness for events at  $\Delta < 40^\circ$ , suggesting increased incoherent scattering for shallow-incidence  $P$  waves.

The Levin and Park (1997a) model posited a shallow low-velocity layer atop the crust, based mainly on a slight time delay of the broad first motion of the transverse RF. Figure 12 confirms this interpretation, as the radial RF sweep indicates a sharp positive-polarity  $P_s$  conversion at  $t \sim 0.4$  sec delay. The thickness of the surface layer may exceed that of the Levin and Park (1997a) model, however. If  $V_p = 5.0$

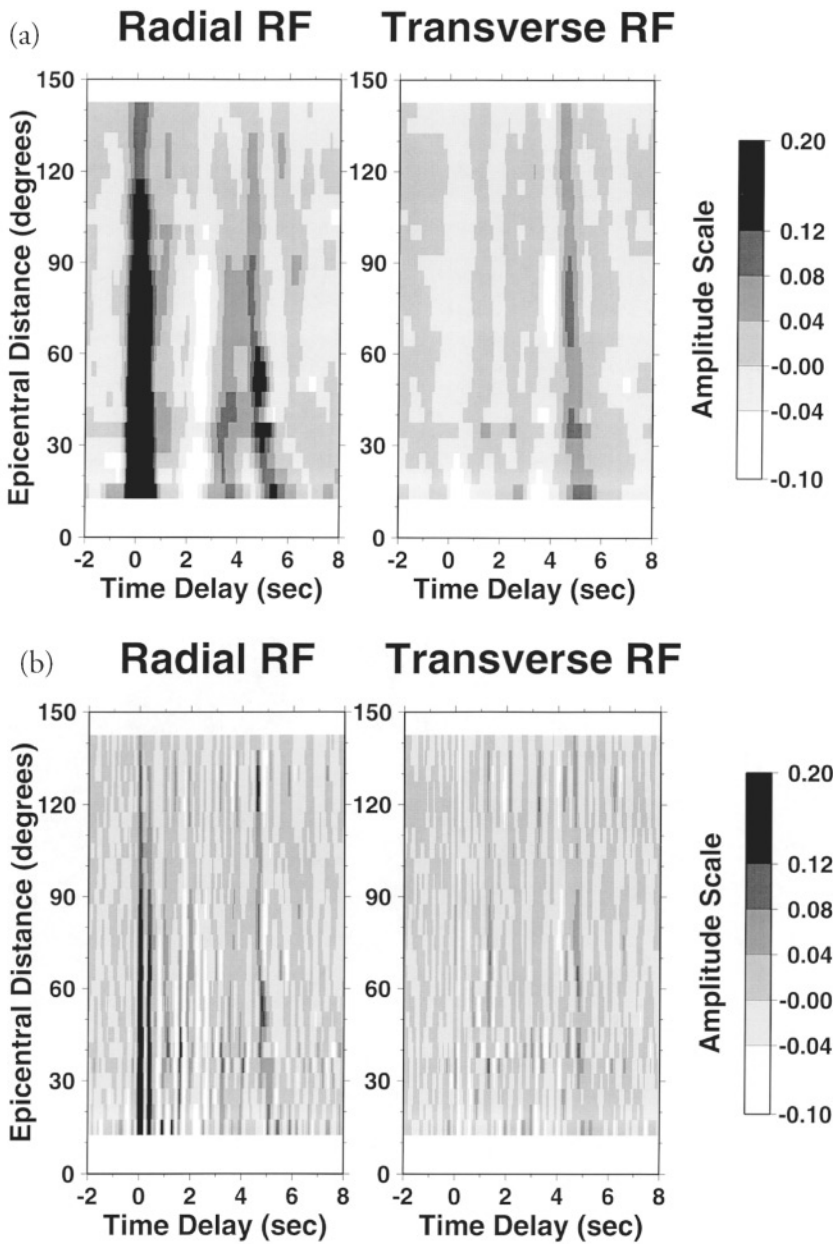


Figure 12. Grey-shade plots of composite RFs at ARU for frequency cutoffs (a)  $f_c = 1.5$  Hz and (b)  $f_c = 6.0$  Hz, plotted against epicentral distance  $\Delta$ . Only events in the backazimuth range  $50\text{--}150^\circ$  contribute to the composite RFs. The composite RFs are computed from a weighted sum of single-event MTC RFs for events in a bin width  $\delta\Delta = 10^\circ$ . The composite RFs are computed with a spacing in  $\Delta$  of  $5^\circ$ , so data from each seismic event influences two adjacent bin-averages.

km/sec and  $V_s = 2.5$  km/sec, then a 2-km surface layer is required to obtain a  $Ps$ -conversion delay of 0.4 sec, assuming vertical incidence. For this somewhat arbitrary choice of parameters, some of the RF wiggles in the first few seconds can be explained as shallow  $SV$  reverberations. For instance, a  $P$ -to- $S$  conversion at the free surface that reverberates once in such a shallow layer would arrive at  $t = 1.6$  sec delay for vertical incidence, in fair agreement with a sharp oscillation in the radial RF sweep for  $\Delta \lesssim 90^\circ$ . Not all energy in this time window need be caused by a shallow-layer reverberation, for example, the positive-polarity signal at  $t \sim 1.3$  sec on the transverse RF sweep. ARU lies atop the foredeep of the Paleozoic Urals collision zone, so coherent horizontal layering of ancient sedimentary layers in the upper crust

would not be surprising. A  $Ps$  conversion at  $t = 1.3$ -sec delay implies an interface at roughly 10 km depth. This is consistent with results from the Vibroseis reflection profile collected 500 km south of ARU along the URSEIS cross-Urals survey line (Echtler *et al.*, 1996). In the URSEIS study, the Urals foredeep shows strong, isolated, horizontally extended reflectors, interpreted to lie at 5, 10, and 15–20 km depth.

The interpretation of receiver functions can be complicated greatly by the presence of shallow (20–200 m) resonances in slow sedimentary layers, whether from organ-pipe reverberations at steep incidence (Hough, 1990) or from Rayleigh waves scattered horizontally by surface topography (Levander and Hill, 1985). Shallow-resonance excita-

tion by a teleseismic *P* wave is not necessarily incoherent scattering and may not be screened out of the MTC RF. An example of this may be evident at GSN station PET, in operation since fall 1993. We computed MTC RFs for 250 seismic *P*-wave records, using data intervals between 50 and 100 sec. PET is somewhat noisier than ARU, but is closer to the seismicity of the Pacific Rim subduction zones. Its average squared-coherence  $C^2(f)$  between horizontal and vertical components of the *P* waves is comparable to ARU, perhaps slightly greater for  $1 < f < 3$  Hz (Fig. 13). More notable are a succession of peaks in  $C^2(f)$  at (roughly)  $f = 0.6, 1.6, 2.4,$  and  $3.2$  Hz. Following Hough (1990), the spaced coherence peaks suggest a sequence of resonant modes in the shallow sediments surrounding the PET vault. The simplest layer-over-halfspace model predicts resonances in the shallow layer according to the quarter-wavelength rule. To satisfy zero traction at the free surface and near-zero displacement at the rock-sediment interface with a vertically incident wave of wavelength,  $\lambda$ , a sequence of leaky-mode “organ-pipe” resonances corresponding to  $1/4\lambda, 3/4\lambda, 5/4\lambda,$  and so forth, exist in the sediment layer. If the quarter-wavelength fundamental resonance oscillates at  $f_0$ , the overtone frequencies for the sequence are  $3f_0, 5f_0, 7f_0,$  etc. The coherence peaks for the MTC RF analysis at PET follow this prediction roughly, suggesting a shallow resonance.

The behavior of the PET radial RFs supports the existence of a shallow resonance, but with additional signal that may arise from *Ps* conversion deeper in the crust. Figure 14 compares radial RFs for  $f_c = 1.5$  Hz and  $f_c = 3.0$  Hz in an epicentral-distance sweep, using events at backazimuths  $150^\circ \leq \psi \leq 250^\circ$ . The RFs for events with  $25^\circ \leq \Delta \leq 95^\circ$  and  $f_c = 1.5$  Hz exhibit several oscillations with period  $\approx 2$  sec. This corresponds to the fundamental resonance frequency ( $\sim 0.6$  Hz) inferred from the coherence peaks in Figure 13. For RFs with cutoff frequency,  $f_c = 3.0$  Hz, the first 6 sec of the radial RF lose their cyclicity, augmented and distorted by short pulses at irregular time intervals. Although a more complex shallow resonance might cause this pattern, it is plausible to expect deeper *P*-to-*S* conversions in the actively deforming crust beneath PET, as it lies on the overriding side of the Kamchatka subduction zone (Gorbatov *et al.*, 1997).

The PET example demonstrates that, although MTC RFs may reject much signal-generated noise, not all features in the MTC RFs may shed light on deeply buried geological structures. Side-scattered energy can, in principle, contribute to the RF as readily as can upward-scattered waves from horizontal interfaces. The moveout of side-scattered energy with either epicentral distance or, more readily, backazimuth, can help distinguish it from other scattered-wave types.

### Summary

Multiple-taper correlation can be used in place of spectral division and time-domain deconvolution to compute RFs

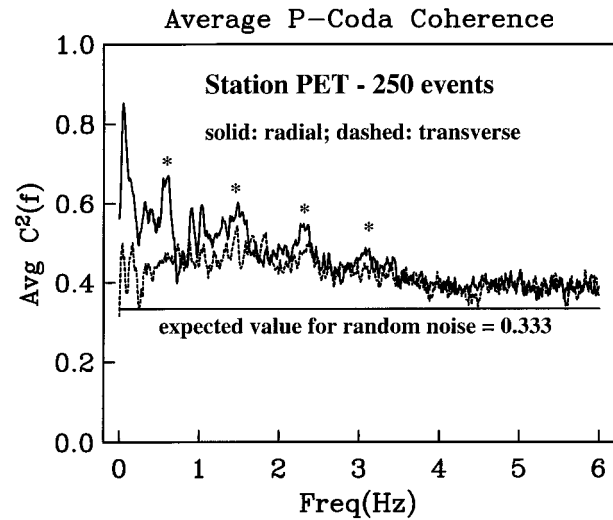


Figure 13. Average squared coherence  $C^2(f)$  for 250 teleseismic *P* coda recorded at PET, between the vertical and radial (solid line) and transverse (dashed line) horizontal components of seismic motion. Asterisks mark a sequence of (roughly) evenly spaced coherence peaks that suggest the influence of a shallow-sediment resonance on the computed receiver functions.

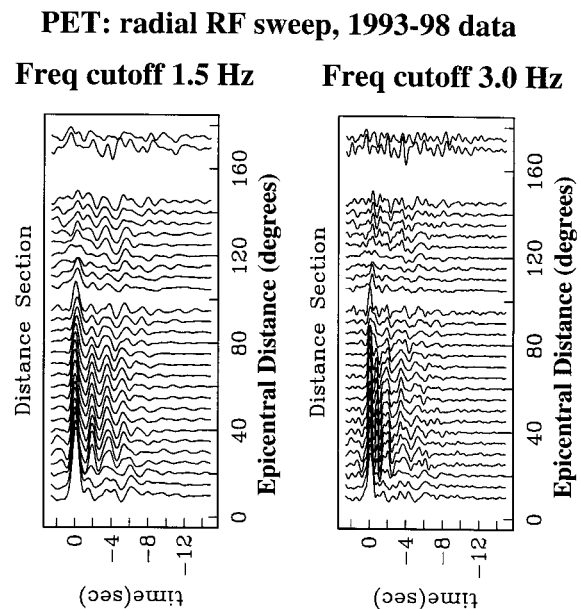


Figure 14. Composite radial RFs for GSN station PET (Petropavlovsk-Kamchatsky, Russia) plotted with epicentral distance. Only events in the backazimuth range  $150\text{--}250^\circ$  contribute to the composite RFs.

from teleseismic  $P$  waves. The MTC method provides an estimate of RF uncertainty in the frequency domain. This enables RFs from different seismic events to be combined in a weighted-average RF estimate, rather than an unweighted stack. The new method appears in test cases to be more resistant to “incoherent” signal-generated noise, which can seriously contaminate RF estimates. Analysis of  $P$ -coda data from two broadband permanent seismic observatories suggests that, on average, at least 33% of the radial-horizontal variance at  $f < 1$  Hz is incoherent with vertical motion and likely to be signal-generated noise, for example, body-to-surface-wave conversions. At high frequencies on the radial component and all frequencies on the transverse component, 50% or more of the variance is likely to be signal-generated noise. Its greater resistance to signal-generated noise allows MTC RF estimates to extend to frequencies well beyond 1 Hz, approaching the effective resolution of active-source deep-crustal seismic studies. The MTC RF estimator may therefore be a useful tool in studies of crust and uppermost mantle structure with portable broadband arrays.

At GSN station ARU atop the foredeep of the Ural Mountains continental suture, MTC RF analysis confirms the broad features of the RFs predicted by the anisotropic crustal model of Levin and Park (1997a) and sharpens the resolution of several  $P$ s converted phases. In particular, the Moho conversion is quite sharp, as is a  $P$ s conversion at the base of a thin ( $\sim 2$ -km) low-velocity surface layer. In an example of “coherent” signal-generated noise, at station PET atop the Kamchatka subduction zone, MTC RF estimates appear to be overprinted by a  $\sim 2$ -sec resonance in shallow sediments.

### Acknowledgments

This work was supported by Defense Threat Reduction Agency Contract DSWA01-98-011. We used GMT software (Wessel and Smith, 1991) to prepare some figures. Comments by Frank L. Vernon III and an anonymous reviewer helped us clarify some points in the text.

### References

- Abers, G. A. (1998). Array measurements of phases used in receiver-function calculations: importance of scattering, *Bull. Seism. Soc. Am.* **87**, 313–318.
- Abers, G. A., X. Hu, and L. R. Sykes (1995). Source scaling of earthquakes in the Shumagin region, Alaska: time-domain inversions of regional waveforms, *Geophys. J. Int.* **123**, 41–58.
- Ammon, C. J. (1991). The isolation of receiver effects from teleseismic  $P$  waveforms, *Bull. Seism. Soc. Am.* **81**, 2504–2510.
- Ammon, C. J., G. E. Randall, and G. Zandt (1990). On the nonuniqueness of receiver function inversions, *J. Geophys. Res.* **95**, 15,303–15,318.
- Baker, E. G., J. B. Minster, G. Zandt, and H. Gurrola (1996). Constraints on crustal structure and complex Moho topography beneath Pinon Flat, California, from teleseismic receiver functions, *Bull. Seism. Soc. Am.* **86**, 1830–1844.
- Bostock, M. G. (1997). Anisotropic upper-mantle stratigraphy and architecture of the Slave craton, *Nature* **390**, 393–395.
- Bostock, M. G., and M. D. Sacchi (1997). Deconvolution of teleseismic recordings for mantle structure, *Geophys. J. Int.* **129**, 143–152.
- Burdick, L. J., and C. A. Langston (1977). Modeling crustal structure through the use of converted phases in teleseismic body-wave forms, *Bull. Seism. Soc. Am.* **67**, 677–691.
- Cassidy, J. F. (1992). Numerical experiments in broadband receiver function analysis, *Bull. Seism. Soc. Am.* **82**, 1453–1474.
- Clayton, R. W., and R. A. Wiggins (1976). Source shape estimation and deconvolution of teleseismic body waves, *Geophys. J. R. Astron. Soc.* **47**, 151–177.
- Dueker, K. D., and A. F. Sheehan (1997). Mantle discontinuity structure from midpoint stacks of converted  $P$  to  $S$  waves across the Yellowstone hotspot track, *J. Geophys. Res.* **102**, 8313–8327.
- Eaton, D. W., and J. F. Cassidy (1996). A relict Proterozoic subduction zone in Western Canada: new evidence from seismic reflection and receiver function data, *Geophys. Res. Lett.* **23**, 3791–3794.
- Echtler, H. P., M. Stiller, F. Steinhoff, C. Krawczyk, A. Suleimanov, V. Spiridonov, J. H. Knapp, Y. Menshikov, J. Alvarez-Marron, and N. Yunusov (1996). Preserved collisional crustal structure of the southern Urals revealed by Vibroseis profiling, *Science* **274**, 224–226.
- Gorbatov, A., V. Kostoglodov, G. Suarez, and E. Gordeev (1997). Seismicity and structure of the Kamchatka subduction zone, *J. Geophys. Res.* **102**, 17,883–17,898.
- Gurrola, H., and J. B. Minster (1998). Thickness estimates of the upper-mantle transition zone from bootstrapped velocity spectrum stacks of receiver functions, *Geophys. J. Int.* **133**, 31–43.
- Gurrola, H., F. G. Baker, and J. B. Minster (1995). Simultaneous time-domain deconvolution with application to the computer of receiver functions, *Geophys. J. Int.* **120**, 537–543.
- Hough, S. E. (1990). Constraining sediment thickness in the San Francisco Bay area using observed resonances and  $P$ -to- $S$  conversions, *Geophys. Res. Lett.* **17**, 1469–1472.
- Kosarev, G. L., Makeyeva, L. I., and Vinnik, L. P. (1984). Anisotropy of the mantle inferred from observations of  $P$  to  $S$  converted waves, *Geophys. J. R. Astron. Soc.* **76**, 209–220.
- Kosarev, G., R. Kind, S. V. Sobolev, X. Yuan, W. Hanka, and S. Oreshin (1999). Seismic evidence for a detached Indian lithospheric mantle beneath Tibet, *Science* **283**, 1306–1309.
- Kuo, C., C. R. Lindberg, and D. J. Thomson (1990). Coherence established between atmospheric carbon dioxide and global temperature, *Nature* **343**, 709–713.
- Langston, C. A. (1981). Evidence for the subducting lithosphere under southern Vancouver Island and western Oregon from teleseismic  $P$  wave conversions, *J. Geophys. Res.* **86**, 3857–3866.
- Lees, J., and J. Park (1995). Multiple-taper spectral analysis: a stand-alone C-subroutine, *Computers and Geosciences* **21**, 199–236.
- Levander, A. R., and K. Hill (1985).  $P$ - $SV$  resonances in irregular low-velocity surface layers, *Bull. Seism. Soc. Am.* **75**, 847–864.
- Levin, V., and J. Park (1997a). Crustal anisotropy beneath the Ural mtns foredeep from teleseismic receiver functions, *Geophys. Res. Lett.* **24**, 1283–1286.
- Levin, V., and J. Park (1997b).  $P$ - $SH$  conversions in a flat-layered medium with anisotropy of arbitrary orientation, *Geophys. J. Int.* **131**, 253–266.
- Levin, V., and J. Park (1998). A  $P$ - $SH$  conversion in layered media with hexagonally symmetric anisotropy: a cookbook, *Pure Appl. Geophys.* **151**, 669–697.
- Levin, V., and J. Park (2000). Shear zones in the Proterozoic lithosphere of the Arabian Shield and the nature of the Hales discontinuity, *Tectonophysics* **323**, 131–148.
- Levin, V., W. Menke, and J. Park (1999). Shear wave splitting in Appalachians and Urals: a case for multilayered anisotropy, *J. Geophys. Res.* **104**, 17,975–17,994.
- Owens, T. J., and R. S. Crosson (1988). Shallow structure effects on broadband teleseismic  $P$  waveforms, *Bull. Seism. Soc. Am.* **77**, 96–108.
- Park, J. (1996). Surface waves in layered anisotropic structures, *Geophys. J. Int.* **126**, 173–184.
- Park, J., Lindberg, C. R., and F. L. Vernon III (1987). Multitaper spectral analysis of high-frequency seismograms, *J. Geophys. Res.* **92**, 12,675–12,684.

- Regnier, M. (1988). Lateral variation of upper mantle structure beneath New Caledonia determined from *P*-wave receiver function; evidence for a fossil subduction zone, *Geophys. J. R. Astron. Soc.* **95**, 561–577.
- Sandvol, E., D. Seber, A. Calvert, and M. Barazangi (1998). Grid search modeling of receiver functions: implications for crustal structure in the Middle East and North Africa, *J. Geophys. Res.* **103**, 26,899–26,917.
- Savage, M. (1998). Lower crustal anisotropy or dipping boundaries? Effects on receiver functions and a case study in New Zealand, *J. Geophys. Res.* **103**, 15,069–15,087.
- Searcy, C. K., D. H. Christensen, and G. Zandt (1996). Velocity structure beneath College Station Alaska from receiver functions, *Bull. Seism. Soc. Am.* **86**, 232–241.
- Sheehan, A. F., G. A. Abers, C. H. Jones, and A. L. Lerner-Lam (1995). Crustal thickness variations across the Colorado Rocky Mountains from teleseismic receiver functions, *J. Geophys. Res.* **100**, 20,391–20,414.
- Thomson, D. J. (1982). Spectrum estimation and harmonic analysis, *IEEE Proc.* **70**, 1055–1096.
- Vernon, F. L., J. Fletcher, L. Carroll, A. Chave, and E. Sembrera (1991). Coherence of seismic body waves from local events as measured by a small-aperture array, *J. Geophys. Res.* **96**, 11,981–11,996.
- Vinnik, L. P., and J.-P. Montagner (1996). Shear wave splitting in the mantle *Ps* phases, *Geophys. Res. Lett.* **23**, 2449–2452.
- Wessel, P., and W. H. F. Smith (1991). Free software helps map and display data, *EOS Trans. AGU* **72**, 441.

Dept of Geology and Geophysics  
Yale University  
PO Box 208109  
New Haven, Connecticut 06520-8109

Manuscript received 3 September 1999.